A time-average filtering technique to improve the efficiency of Two-Layer Wall Models for Large Eddy Simulation in complex geometries.

J. Calafell[a,b], F.X. Trias[a], O. Lehmkuhl[a,b], A. Oliva[a]

[a] *Heat and Mass Transfer Technical Center (CTTC). Technical University of Catalonia (UPC), Colom 11, 08222 Terrassa (Barcelona), Spain*
[b] *Termo Fluids S.L. Avda. Jacquard 97 1-E, 08222 Terrassa (Barcelona),Spain*

Abstract

Two-Layer wall models have been recurrently studied since they represent a good physical model for Large Eddy Simulations with underresolved wall regions. Specifically, those based on the Reynolds Averaged Navier-Stokes equations are of special interest, since they can be applied to a wide range of conditions including non-equilibrium flows. Nonetheless, these models are affected by two recurrent problems, the "log-layer mismatch" and the resolved Reynolds stresses inflow, which until now, have been dealt with separated techniques. In this work, a time-filtering methodology is applied to tackle both issues at once with a single and low-computational-cost step, easily applicable to complex three-dimensional geometries. The time-filtering technique has already been applied to other types of wall models to mitigate the "log-layer mismatch." Now, it is applied for the first time in the Two-Layer wall model context, showing its ability not only in avoiding the mismatch issue but also in blocking the resolved Reynolds stress inflow, dramatically

Email address: joancs@cttc.upc.edu (J. Calafell)

improving the wall model performance and generality compared to other existing implementations. A methodology to determine the necessary temporal filter length is proposed and validated in equilibrium and non-equilibrium conditions. Additionally, the filter size influence on large-scale unsteady flow motions is assessed. Good results are obtained in steady and unsteady flow regimes by suppressing the LES highest frequencies while taking into account large-scale temporal effects.
Keywords: Large Eddy Simulation, Wall Modeling, Two-Layer Model, Time-Filtering, Boundary Layer

1. Introduction

The modelization of high Reynolds number wall-bounded flows is of great interest since they are present in a wide range of fundamental industrial areas ranging from the wind energy industry to the aerospace or automotive sectors among others. Unfortunately, accurate numerical simulations of wall-bounded flows at high Reynolds number are extremely demanding from a computational cost viewpoint, making the industry to mainly rely on low fidelity computational fluid dynamics (CFD) techniques or experimental methodologies for aerodynamic design.

The physical explanation for such a great difficulty is found in the near-wall flow structure. Boundary layers enclose a vast range of different motion scales. Since the behavior of the small inner layer structures has substantial implications on the development of the outer layer and by extension on the far field region, a sufficiently fine mesh is required in the near-wall area to capture them. This physical phenomenon is extremely challenging since the

structures located in the inner layer become smaller as the Reynolds number increases entailing massive requirements in terms of spatial and temporal resolution.

The development of new mathematical models and improvements in algorithmic efficiency may result in substantial cost reductions in numerical predictions, making accurate simulations affordable. The classical approaches used to deal with high Reynolds number flows (both, wall-bounded and free flows) have historically been the Reynolds averaged Navier-Stokes (RANS) and the large eddy simulation (LES) methodologies. Unfortunately, although RANS is a conventional methodology for aerodynamic optimization and design given its relatively low computational cost, it suffers from a lack of generality leading in many cases to poor quality results. On the other hand, LES has still a prohibitive computational cost[1] due to the large amount of spatial and temporal resolution required which hampers the spread of its use throughout the industry.

In this context, wall modeling for LES in which the present work is focused aims at taking advantage of the LES accuracy while minimizing the computational costs derived from the complex near-wall flow physics.

Some works intended to quantify the gains of using wall-modeled LES (WMLES) instead of wall-resolved LES (WRLES) concerning mesh requirements, can be found in the literature. Chapman [2] published a first approximation in 1979 concluding that, for a WRLES (i.e., inner layer resolution) the total number of grid points, N, is proportional to $Re_{L_x}^{9/5}$. By contrast, for a WMLES (i.e., outer layer resolution only) the mesh resolution is proportional to $Re_{L_x}^{2/5}$. These estimates were based on a turbulent boundary layer

over a flat plate case, being L_x the plate length in the streamwise direction. Choi and Moin[3] updated the Chapman estimates by using more recent studies on the skin friction coefficient and boundary layer thickness. They concluded that the WRLES requires a number of grid points proportional to $Re_{L_x}^{13/7}$, while the WMLES only required a number proportional to Re_{L_x}. On the other hand, in the studies conducted by Chapman, only a slight mention to the Reynolds number scaling of the time-step was made with no further development, whereas in the works carried out by Choi and Moin, the time-step restriction was not taken into account. Nonetheless, this issue is also of capital importance, and probably even more challenging than the number of grid points since parallelization of temporal evolution, although it is a current research topic[4], is of great difficulty.

In this regard, a set of expressions approximating the Reynolds number scaling of the upper bound of the computational time-step size, Δt, is proposed hereafter. It is straightforward to show that the computational cell volume, v_{cell}, is inversely proportional to the number of grid points, N_V, in a given volume, V, when the same assumptions of Chapman and Choi and Moin apply. This volume V may be either a portion of the outer region of a boundary layer or a sample of the inner viscous layer. This can be expressed as $v_{cell} \sim 1/N_V$, and using the scalings proposed by Choi and Moin in terms of grid points, we find that:

$$v_{cell}^{WM} \sim Re_{L_x}^{-1}, \tag{1}$$

$$v_{cell}^{WR} \sim Re_{L_x}^{-13/7}. \tag{2}$$

The CFL requirements set two different upper bounds for the time-step,

one for the convective, Δt_c, and another for the diffusive term, Δt_d, being used the most restrictive at each computational step. It should be pointed out that the CFL time-step is small compared to the smallest physical time-scales supported by a given mesh, which ensures that the accuracy is limited by the spatial resolution rather than the temporal one . This applies for flows in which eddies deform at a rate significantly smaller than the maximum velocity in the computational domain which holds for a large number of turbulent flows [5]. For structured meshes, the CFL bounds are expressed as:

$$\Delta t_c = C_{conv} \left| \frac{\Delta x_i}{u_i} \right|_{min}, \tag{3}$$

$$\Delta t_d = C_{diff} \left| \frac{\Delta x_i^2}{\nu} \right|_{min}, \tag{4}$$

where C_{conv} and C_{diff} are two constants which depend on the time integration scheme, ν is the kinematic viscosity, the i subindex stands for the spatial coordinates, Δx_i is the grid spacing and u_i is the velocity component. For unstructured meshes the grid spacing is approximated according to the classical Deardorff definition[6], $\Delta x_i = v_{cell}^{1/3}$, while u_i is replaced by the velocity magnitude. Combining equations (1)-(2) and (3)-(4), we find four expressions for Δt:

$$\Delta t_c^{WM} \sim Re_{Lx}^{-1/3} \quad , \quad \Delta t_d^{WM} \sim Re_{Lx}^{-2/3}, \tag{5}$$

$$\Delta t_c^{WR} \sim Re_{Lx}^{-13/21} \quad , \quad \Delta t_d^{WR} \sim Re_{Lx}^{-26/21}, \tag{6}$$

where Δt_c^{WM} and Δt_d^{WM} are the upper bound of the time-step for the convective and the diffusive terms in WMLES while Δt_c^{WR} and Δt_d^{WR} are the

same values but for WRLES. The scaling laws vary strongly depending on which restriction prevails, the convective or the diffusive one. Nevertheless, for a given Re_{Lx}, the more restrictive diffusive bound gets dominant over the convective one as the mesh is refined [7]. Hence, in WMLES, the time-step upper bound scales closer to $Re_{Lx}^{-1/3}$ while in WRLES, the Δt scales nearly as $Re_{Lx}^{-26/21}$.

Nonetheless, the feasibility of a particular computation depends on the combined costs related to the number of grid points and the time-step size. We define the non-dimensional variable T_{cc} which stands for the total computational cost of a given computation. We are not interested in quantifying its value but to determine its scaling with the Reynolds number. Considering an ideal code, the computational cost would be proportional to the number of grid points ($T_{cc} \sim N$), while if a direct solver is considered for the Poisson equation, the computational cost per time-step would be also inversely proportional to the time-step size ($T_{cc} \sim 1/\Delta t$). Combining both scaling laws and replacing the N and Δt values for the WMLES and WRLES Reynolds scaling expressions respectively, we obtain:

$$T_{cc}^{WM} \sim N \frac{1}{\Delta t} = Re_{Lx} \frac{1}{Re_{Lx}^{-1/3}} = Re_{Lx}^{4/3} \tag{7}$$

$$T_{cc}^{WR} \sim N \frac{1}{\Delta t} = Re_{Lx}^{13/7} \frac{1}{Re_{Lx}^{-26/21}} = Re_{Lx}^{65/21} \tag{8}$$

where T_{cc}^{WM} and T_{cc}^{WR} are the total computational cost in a WMLES and in a WRLES computation, respectively. While the total computational cost scaling of a WMLES suffers a slight change when considering the time-integration contribution compared to the Choi and Moin estimates (from Re_{Lx} to $Re_{Lx}^{1.33}$),

in a WRLES the T_{cc} scaling increases dramatically from approximately $Re_{Lx}^{1.85}$ to $Re_{Lx}^{3.09}$. These new expressions highlight even more the extreme difficulty of performing WRLES computations of industrial relevant Reynolds numbers.

After reviewing the difficulties that arise when dealing with WRLES, it is clear that WMLES is a very promising strategy to make wall flow computations at high Reynolds number affordable. Several approaches have been developed since the nineties, but all of them are based on modeling the inner layer in one way or the other instead of fully resolving it from a temporal and spatial point of view. These strategies can be mainly split into two major subgroups, hybrid RANS-LES models, and wall shear stress methods. The main conceptual difference between both methodologies is that in hybrid RANS-LES, the wall model (WM) is embedded in the turbulence model itself. The model returns a RANS-type turbulent viscosity in the near-wall regions while it switches to an LES-type subgrid viscosity in the outer layer and the far field regions. On the other hand, in wall shear stress methods, an LES model is solved down to the wall while a shear stress is provided by an external model to the LES domain as a boundary condition. The main differences and the range of applicability of these methodologies were discussed in more detail by Piomelli[1] in 2008, while a complete review of the hybrid RANS-LES techniques and their continuous improvements was published by Spalart et al.[8] in 2009.

1.1. Two-layer models

This paper is focused in the wall shear stress strategy and in particular, the zonal or two-layer model (TLM) approach proposed by Balaras *et al.* [9, 10] in the mid-'90s. This methodology is based on the resolution of the RANS

equations or a simplified variant in a fine auxiliary mesh that is embedded in the LES domain between the solid boundary and the first off-wall node (see Figure 1). The boundary conditions are taken from the LES nodes while the time integration is carried out with implicit or semi-implicit schemes to avoid restrictions due to stability considerations.

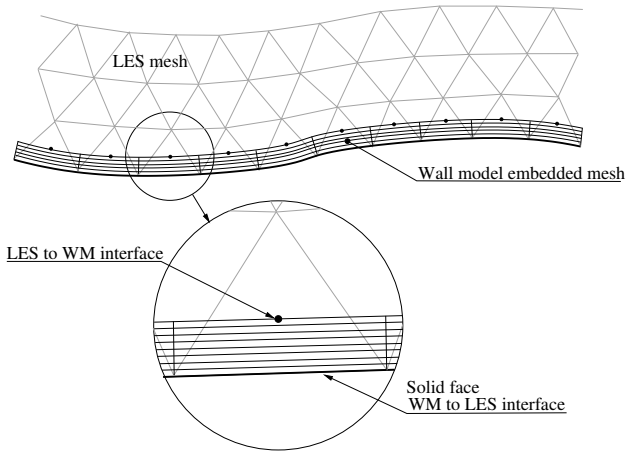

Figure 1: The two-layer strategy scheme.

With increasing complexity of the near-wall governing equations, fewer assumptions are made compared to other methodologies such as wall functions in which an a priori known velocity profile is assumed [11]. Once the near-wall velocity profile is established, an accurate wall shear stress, τ_w, can be evaluated and fed back into the LES domain. In the initial works[9, 10], the two-dimensional turbulent boundary layer equations (TBLE) were solved. These equations are derived from the RANS ones by assuming the non-variation of the pressure in the wall-normal direction (i.e., $\partial P/\partial n = 0$) whereas only the variation of the velocity in the wall-normal direction is considered for the diffusive term. To close the formulation, a simple mixing-length eddy

viscosity model with a damping function was used to evaluate the turbulent viscosity, ν_t. In the initial work, Balaras *et al.*[9, 10] achieved promising results in the numerical tests performed. However, only equilibrium flows were tested (channel and duct flow) and they suggested to carry out further tests with strong adverse pressure gradients and separated regions. From the initial concept, different authors have suggested variants and improvements, and the idea is still being developed.

Later, Cabot *et al.* [12, 13] carried out computations on a backward-facing step. They found that the total amount of Reynolds stresses (resolved+modeled) in the wall layer was overestimated when using the TBLE-based (non-equilibrium) model causing an overprediction of the skin friction coefficient C_f.

Resolved turbulent motions and their associated fluctuating velocity field have inherent diffusive effects on the mean flow [14]. In the Navier-Stokes physical model, these effects are not explicitly introduced but they are an indirect consequence of the time-resolved fluctuations. Following Pope's nomenclature, this source of diffusivity will be named as apparent diffusivity. On the other hand, when turbulent scales are not fully resolved, their diffusive effects can be introduced through a model. This source of diffusivity is named as modeled diffusivity, and unlike the apparent one, it is explicitly introduced through an extra viscosity added to the diffusive term. The RANS approach is intended to exclusively resolve the mean flow, while the effects of the whole fluctuating component (Reynolds stresses) are modeled through the turbulent viscosity, ν_T. Therefore, if additional time-resolved fluctuations are introduced in a RANS domain through the boundary by the

advective term, their apparent diffusive effects will be added to the RANS modeled ones, which already account for the whole fluctuating field. This causes the overprediction pointed out by Cabot et al. From here onwards, this effect will be named as resolved Reynolds stresses inflow (RRS inflow).

To counteract this effect, the authors proposed a modified mixing-length turbulence model in which the Von Kármán constant, κ, was adjusted dynamically to reduce the modeled Reynolds stresses contribution. This correction allowed to obtain better results in the skin friction prediction. They also tested the so-called "stress balance model" which neglects the pressure gradient and advective terms of the TBLE equations. They found that while the mean velocity profiles were relatively well resolved compared with the WR-LES, the model failed in predicting the C_f in the separated region or in the presence of strong pressure gradients. The results showed that neglecting the advective and pressure gradient terms was an unreasonable assumption when it comes to non-equilibrium flows. All these results were confirmed in subsequent works. Namely, Wang [15] performed computations of a trailing-edge flow reaching similar conclusions with both models, the equilibrium (only diffusive and temporal terms) and the full TBLE one. Especially good results were obtained for the skin friction coefficient when using the dynamic correction proposed by Cabot[12] compared to the ones obtained with a constant κ in which the C_f was overestimated. Later, Tessicini [16, 17] performed computations of flows with more complex geometries, such as a fully three-dimensional (3D) circular hill. The equilibrium model was tested together with a variant of the TBLE model which only neglected the advective term, making clear again the need for the non-equilibrium terms in separated flow

regions. Finally, the same conclusion was reached by Kawai *et al.* [18] when computing the flow around an airfoil near stall condition.

The equilibrium assumption is also implicit with the use of a mixing-length eddy viscosity model. Diurno *et al.* [19] also computed a backward-facing step case but using the Spalart Allmaras (SA) model[20] in the wall layer to override the equilibrium assumption. Even though the overprediction of Reynolds stresses pointed out by Cabot[12] concerns any RANS model, they found that the WM performed slightly better in the separated regions regarding the C_f prediction when using SA instead of the simple mixing-length with constant κ. However, no evident improvements were obtained in other quantities such as the mean velocity profiles. For more details, the reader is referred to the extensive review of wall-layer modeling published by Piomelli and Balaras [21] in 2002.

From 2010 onwards, new efforts have been carried out to improve the TLM strategy. Some of the previous works pointed out the impossibility of having accurate LES velocity data at the first few off-wall nodes, mainly due to the use of inadequate LES models and large numerical errors in the near-wall region when using coarse meshes [13]. These errors were supposed to cause the so-called "log-layer mismatch" (LLM) error, an unphysical rise of the fluid velocity in the boundary layer logarithmic region. Kawai and Larsson [22, 23] stretched the wall layer mesh beyond the first off-wall node, reducing numerical and subgrid modeling errors caused by the wall proximity and suppressing the LLM issue. This methodology allowed to obtain excellent results in the LES domain for points beyond the WM/LES interface. However, the extended wall layer domain entails significant computational

costs due to a large number of required grid points while causing serious geometrical difficulties when generating the TLM mesh in complex geometries. Although in a different context than TLM, recent works proposed alternative methodologies to deal with the LLM issue. Yang *et al.* [24] applied a time-averaging filter (TAF) to a simple logarithmic-law-like equilibrium wall model. Good results were reported in the mean velocity profile of a high Reynolds Channel Flow, even taking LES data from the first off-wall node. The authors argued that when using data from the Δy_1 nodes, the wall shear stress, and the LES velocity fluctuations are artificially in phase. This instantaneous synchronization is unphysical and causes unreal damping of the Reynolds shear stresses ($-\langle u'v' \rangle$) near the wall. This effect is compensated by a rise of the velocity gradient ($\langle \partial u/\partial y \rangle$) to fulfill the momentum balance in the first off-wall nodes of a channel flow with a constant pressure gradient ($-\langle u'v' \rangle + \langle (\nu + \nu_{sgs})\, \partial u/\partial y \rangle) = (1/\rho)\partial p/\partial x = ct$). According to the authors, the reason why the application of a TAF eliminates the LLM, is that the temporal coupling between the first off-wall LES velocity and the wall shear stress is broken, eliminating the unphysical damping of the Reynolds shear stresses. This also explains the ability of Kawai's methodology in preventing the LLM since taking the LES data away from the wall, also eliminates the artificial synchronization.

Kawai and Larsson also reviewed the skin friction overprediction issue derived from the RRS inflow. They proposed a new approach to evaluate the κ coefficient [22, 18, 25] in the TLM turbulence model. They showed that κ could not remain constant in the wall-normal direction given that the ratio between resolved/modeled Reynolds stressed varies dramatically in

that direction. They argued that the wall-parallel resolution was fine enough to resolve turbulent scales from a given wall separation since the size of the near-wall turbulent structures is proportional to the wall distance. As the wall-parallel grid spacing gets smaller with respect to the wall-normal distance, the contribution of resolved stresses to the total ones rises, and the modeled part must be lowered to avoid overpredictions. Both contributions, the stretched mesh and the variable κ were successful in predicting mean velocity profiles and turbulence statistics in various tests, such as a turbulent boundary layer and a compressible shock/boundary-layer interaction among others. Nevertheless, the dynamic procedure proposed by Kawai and Larsson[22, 18, 25] was dependent on a model coefficient that indicated the height at which the generation of resolved stresses began. To circumvent this, a parameter-free model was proposed by Park and Moin [26]. In this approach, the apparent diffusive effects of the incoming resolved Reynolds stresses were explicitly modeled and quantified through a viscous-like quantity, ν_{Pa}, and subsequently subtracted to the RANS turbulent eddy viscosity, keeping appropriate diffusivity levels within the wall layer. However, this approach required a spatial average of the variables along a homogeneous direction to obtain the resolved Reynolds stress tensor component, which severely restricted the generality of the model regarding the allowed geometries [26, 27]. In the latest implementations of TLM[18, 25, 26], the full unsteady RANS compressible equations have been used instead of the TBLE ones which were typically used so far, in order to generalize the method and to take into account all the non-equilibrium phenomena.

Another factor to take into account was the generalization of the method

for any geometry. Patil *et al.* [28] solved the TBLE equations in a generalized coordinate system that allowed the model to adapt to complex geometries. On the other hand, Bodart and Larsson [29] developed a numerical strategy to implement the methodologies proposed by Kawai and Larsson[22, 18, 25] for unstructured meshes. The strategy was followed by Park and Moin [26] who tested their model on a NACA 4412 airfoil at the angle of attack of 12°, in which the laminar to turbulent transition was taken into account by switching off the RANS ν_t in the laminar region by using a turbulent kinetic energy sensor [30]. Reasonably good results were obtained regarding mean velocity profiles and pressure coefficient C_p. A complete review of wall modeling and in particular of two-layer models was published by Larsson *et al.*[27] in 2015.

The present work aims at going further into the generalization of the TLM approach to allow its application in a range of flows as wide as possible, especially to those with practical industrial applications such as high Reynolds number aerodynamics in complex geometries. To do so, an improved and efficient two-layer wall model based on the full incompressible unsteady Reynolds-averaged Navier-Stokes (URANS) equations is proposed for unstructured meshes. The model features a time-averaging filter (TAF) in the WM/LES interface. As previously commented, this approach was firstly introduced by Yang *et al.* for a simple equilibrium wall function, obtaining promising results in suppressing the LLM issue. In the present paper, the TAF technique is applied for the first time to a TLM. In this context, the mission of the TAF is not only suppressing the LLM, but also to block the RRS inflow. It is the first time that a TAF is used for this purpose. More-

over, a methodology to determine the optimal temporal filter length for a RANS-based TLM is proposed.

Firstly, in Section 2, the LES and WM mathematical and numerical strategies are detailed. Then, in Section 3, the ability of the TAF in filtering the incoming RRS from the LES solution is evaluated through a numerical test based on WRLES Pipe Flow at $Re_\tau \approx 500$. Afterward, in Section 4, the model is validated in equilibrium and non-equilibrium conditions with a canonical turbulent Pipe Flow at $Re_\tau \approx 3000$ (Section 4.1) and a stalled DU91-W2-250 airfoil at $Re = 3 \times 10^6$ (Section 4.2), respectively. The effects of the filter length on the numerical predictions are analyzed, including its influence on transient phenomena such as the airfoil boundary layer detachment/reattachment process. Numerical results are compared with direct numerical simulation (DNS) and experimental data depending on the case. Finally, conclusions are given in Section 5.

2. Mathematical and numerical model

In this section, the governing equations and their numerical resolution methods are presented for the LES and the wall model domains.

2.1. The LES mathematical formulation and numerical resolution

In the LES approach, the filtered Navier-Stokes (N-S) equations are numerically solved in order to obtain a direct solution for the scales larger than the filter size. The smaller subgrid scales are not solved, thus their important physical effects are taken into account through the subgrid stress tensor. The LES equations are obtained by spatially filtering the incompressible N-S equations:

$$\nabla \cdot \overline{\mathbf{u}} = 0, \tag{9}$$

$$\frac{\partial \overline{\mathbf{u}}}{\partial t} + (\overline{\mathbf{u}} \cdot \nabla)\, \overline{\mathbf{u}} + \nabla \overline{p} - \nu \nabla^2 \overline{\mathbf{u}} = \nabla \cdot \left(\overline{\mathbf{u}}\, \overline{\mathbf{u}}^T - \overline{\mathbf{u}\mathbf{u}^{\mathbf{T}}} \right) \approx -\nabla \cdot \tau(\overline{\mathbf{u}}), \tag{10}$$

where $\overline{(\cdot)}$ is a spatial commutative filtering operator, $\mathbf{u}$ the velocity field, p the kinematic pressure and $\tau(\overline{\mathbf{u}})$ the subgrid stress tensor which is modeled according to the Boussinesq hypothesis for incompressible flows:

$$\tau\left(\overline{\mathbf{u}}\right) = -2\nu_{sgs} S(\overline{\mathbf{u}}), \tag{11}$$

where $S(\overline{\mathbf{u}})$ is the rate-of-strain tensor, $S(\overline{\mathbf{u}}) = \frac{1}{2}\left(\nabla \overline{\mathbf{u}} + \nabla \overline{\mathbf{u}}^T\right)$, and ν_{sgs} is the subgrid viscosity. Notice that $\tau\left(\overline{\mathbf{u}}\right)$ is considered traceless without the loss of generality, because the trace can be included as part of the filtered pressure, $\overline{p}$.

To close the formulation, a suitable expression for ν_{sgs} must be provided. Most of the published works related to TLM [10, 13, 23, 26], used the dynamic Smagorinsky model of Moin *et al.* [31] with the modification of Lilly [32]. Therefore, in the present work, the same model will be used to allow comparison with other TLM formulations in the literature.

Regarding the numerical resolution of the filtered N-S equations, it is carried out through the finite volume method. The equations are discretized on a collocated unstructured grid arrangement by using second-order symmetry-preserving schemes [33, 34, 35]. These schemes are conservative, i.e., they preserve the symmetry properties of the continuous differential operators and ensure both, stability and conservation of the kinetic energy balance even at high Reynolds numbers and using coarse grids [36]. On the other

hand, the temporal discretization of the momentum equation has been done through a second-order one-step explicit scheme for the convective and diffusive terms[7], while for the pressure, an implicit first-order scheme has been used. Finally, a fractional-step method is applied to solve the pressure-velocity coupling.

2.2. The wall model mathematical and numerical formulation

In order to model the near-wall flow field, the URANS equations are numerically solved:

$$\frac{\partial \mathbf{U}}{\partial t} + (\mathbf{U} \cdot \nabla)\,\mathbf{U} = \nabla \cdot [2(\nu + \nu_{Twm})S(\mathbf{U})] - \nabla P, \tag{12}$$

Here, the capital letters mean time-averaged variables and ν_{Twm} is the RANS turbulent viscosity for the WM. The resolution is performed in a fine embedded mesh that stretches from the solid wall to a given height. For the validation tests, the extrusion length will be set to match the first off-wall row of nodes height (Δy_1), although it can be a user-defined parameter (see Figure 1). The URANS equations have been chosen in order to have the lowest possible degree of approximation by taking into account all the non-equilibrium terms.

To complete the model, a RANS model must be selected to evaluate ν_{Twm}. A mixing-length-based algebraic model together with the Van Driest wall-damping function is used like in most of TLM implementations found in the literature[10, 26]:

$$\nu_{Twm} = (\kappa y)^2 \,|S| \left[1 - exp\left(-y^+/A^+\right)\right]^2, \tag{13}$$

where $\kappa = 0.41$ is the von Kármán constant, y is the wall distance, $|S|$ is the magnitude of the rate-of-strain tensor and $A^+ = 26$, is a constant of the wall-damping function. The superindex + denotes a magnitude in wall units. Even though the law of the wall is implicit in this approach and therefore not valid for non-equilibrium flows, successful results have been reported in several works [18, 26] when using it.

In the introduction, the LLM and the RRS inflow problems were discussed, including their resolution methodologies proposed so far. As previously commented, in the present work, a TAF is applied in the WM/LES interface to tackle both issues at once, with a single and low-computational-cost methodology.

The average filtering of the LES variables is carried out through a numerical exponential running average method[26, 37], which is defined as follows for a given variable ϕ:

$$\overline{\phi}^n = (1-\epsilon)\overline{\phi}^{n-1} + \epsilon\phi^n \quad ; \quad \epsilon = \frac{\Delta t/T}{1+\Delta t/T}, \tag{14}$$

where $\overline{(\cdot)}$ is the time filtering operator, Δt is the time-step at iteration n, and T is the filter characteristic time-scale or filter length. The filtering operation in equation 14 is the numerical solution to the ordinary differential equation $\partial\overline{\phi}/\partial t = (\phi - \overline{\phi})/T$, whose exact solution is $\overline{\phi}(t) = \int_0^t \phi(\xi)\frac{exp[(\xi-t)/T]}{T}d\xi$ [26]. Therefore, $\overline{\phi}$ may be considered as the local time-average of ϕ with an exponential decaying memory, being the decaying speed dependent on the value of T.

The optimal value of T is widely discussed in subsequent sections. Specifically, in Section 3, the minimum necessary filter length allowing to avoid the

RRS inflow is determined through a numerical experiment. Then, in the validation Section 4, the influence of T on the numerical results of both, mean and unsteady magnitudes is evaluated.

Regarding the numerical resolution of the model Equations (12), the finite volume method is applied. Second-order symmetry-preserving numerical schemes have been used to carry out the spatial discretization of the convective term, while a second-order central difference scheme has been applied for the diffusive one. The velocity-pressure coupling has been solved through a projection method while the temporal integration is carried out by means of the Euler first-order implicit scheme. The present implicit projection method includes a pressure-correction step to allow second-order accuracy in the pressure field resolution[38]. The implicit approach is used to avoid numerical stability issues given that the time-step used for the WM computation, is the CFL of the LES domain but applied to a much finer mesh.

On the other hand, Dirichlet boundary conditions are prescribed at the top boundary (see Figure 2) for velocities and pressure taking their values from the time-filtered LES variables, whereas, at the solid faces, no-slip and Neumann conditions are applied for velocities and pressure, respectively. Finally, in the case of existing side boundaries in the WM mesh, appropriate boundary conditions must be set depending on the characteristics of each particular case. The side boundaries are generated by extruding the edges of an open surface, and when they are coincident with an LES mesh boundary, the same boundary condition is applied to both surfaces.

In general, it is difficult to control the LES node positions when dealing with unstructured meshes, and a mismatch between the LES and WM nodes

at the interface surface could easily occur. To minimize numerical inaccuracies, a second-order approximation is used to interpolate the LES values to the WM nodes on the wall model top boundary following the methodology proposed by Park and Moin [39]. These interpolations can cause a small mass imbalance which is corrected at each LES iteration to ensure a zero net mass flow through the external boundaries of the WM mesh.

Finally, once the near-wall velocity profile is obtained, an accurate wall shear stress is derived from the expression $\tau_i \approx \mu\, u_{iy_1}/\delta_{y_1}$, and then, it is supplied to the LES computation to evaluate the diffusive term at the solid face. As shown in Figure 2, u_{iy_1} is the i^{th} velocity component at the first off-wall node with respect to a wall-parallel coordinate system ij and δ_{y_1} is the distance between this node and the wall.

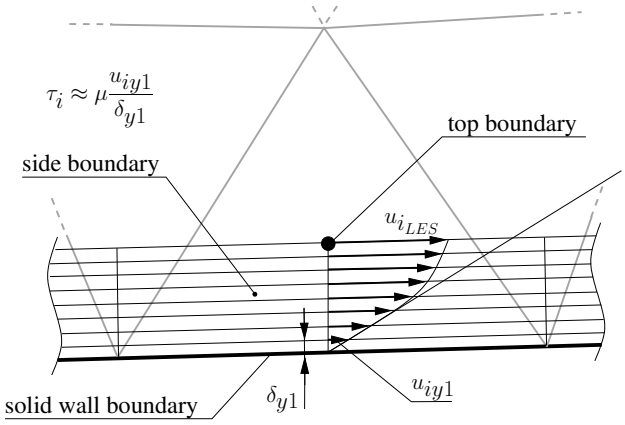

Figure 2: Wall model grid scheme.

2.3. Implementation details

The numerical algorithms used in this work have been implemented in a parallel in-house C++/MPI code called TermoFluids[40]. The parameters

that have to be set to execute the WM are an identifier of the solid surface together with the number of extrusion layers, the WM mesh height, the refinement factor, and the characteristic averaging time-scale T. The vertex topology of the selected solid surface is analyzed, partitioned and uniformly distributed among all the processors to have a proper workload balance. Afterward, the WM mesh is automatically generated by extruding each vertex along a vector obtained by averaging the normal vectors corresponding to all neighboring solid faces. The obtained WM mesh has, therefore, an independent partition with respect to the LES mesh. Hence, a communication pattern between the WM and the solid boundary as well as between the fluid LES nodes and the top WM boundary, is automatically defined and stored since LES to WM communications and vice versa are required at each iteration. Although it is true that having different partitions for the WM and the LES domains requires additional communications for the flow variables and the computed wall shear stress, these additional costs are largely offset by the optimized workload distribution. The alternative would have been that only the processors owning a solid wall portion would be part of the implicit computation of the wall model, which would have generated a massive workload imbalance especially for those cases with small solid surfaces compared to the global computational domain size.

3. Time-averaging filter performance test

In this section, the ability of the TAF in blocking the RRS inflow into the wall layer domain is assessed through a numerical experiment.

The strategy consists in applying the TLM to an independent Pipe Flow

WRLES computation. The WM is fed with time-resolved data taken from the LES domain at the WM/LES interface. This data is used as boundary condition to solve the WM equations but the LES domain is not fed back with the TLM output. Then, the input time-resolved signal is successively filtered with increasing averaging periods, T, to determine the filter length influence on the RRS levels within the WM domain, and the consequences of this on the wall layer physical predictions.

Specifically, the numerical setup is based on a wall-resolved pipe flow at $Re_\tau = u_\tau R/\nu \approx 500$, where R is the pipe radius. Furthermore, the TLM is embedded between the wall and a height of $y^+ \approx 150$, well into the pipe logarithmic law region, which is a plausible operation position of the WM at high Reynolds number. On the other hand, the tested filter lengths are determined by analyzing the power spectrum of the streamwise velocity component at the WM/LES interface. This technique reveals the characteristic time-scales of the flow structures present in that region. These turbulent structures generate the RRS, which are transported into the wall layer through the WM/LES interface causing the wall shear stress overprediction. Since the underlaying behavior of the energy spectrum of a turbulent flow is universal, this methodology will provide a fairly general criterion to establish the necessary filter length for a given flow.

To quantify the presence of RRS in the wall model domain and their apparent diffusive effects, the technique originally proposed by Park and Moin[26] to deal with the diffusivity excess in the TLM context is now used for this other purpose. As commented in the introduction section, Park and Moin modeled the apparent diffusivity inherent to the RRS through a viscosity-

like magnitude, ν_{Pa}, which was subtract to the RANS ν_T to keep appropriate diffusivity levels within the wall layer. Given the physical meaning of ν_{Pa}, its non-dimensional form, ν_{Pa}/ν, is a suitable quantity to measure the apparent diffusive effects of RRS in the WM domain.

According to Park and Moin, the viscous-like quantity, ν_{Pa}, can be obtained with the following expression:

$$\nu_{Pa} = -\frac{R(\mathbf{U})S^d(\mathbf{U})}{2S^d(\mathbf{U})S^d(\mathbf{U})}, \tag{15}$$

where $S^d(\mathbf{U})$, is the deviatoric part of the rate-of-strain tensor, and $R(\mathbf{U})$, is the resolved part of the Reynolds stress tensor. Although the evaluation of $R(\mathbf{U})$ requires the spatial average in an homogeneous direction[26, 27], Equation 15 is applicable for the present test.

On the other hand, the ability of the model in reproducing the flow physics, is evaluated through the mean streamwise velocity profile and the wall shear stress computed by the WM. DNS data of Chin *et al.*[41] is used as a reference for the mean velocity profiles, while the computed Re_τ, is used as a measure of the wall shear stress and compared to the reference value of $Re_\tau \approx 500$.

3.1. Test setup

The WRLES computations are performed in a domain of length $8R$. This is well above the minimum length of $2\pi R$ required to accurately resolve the one-point first and second-order statistics[41] at $Re_\tau \approx 500$. The computational mesh has been generated by extruding a plane mesh along the streamwise direction. The two-dimensional (2D) mesh is a structured mesh with

square-shaped control volumes (CV) in the region between $r = 0.5R$ and $r = R$ while between the pipe center and $r = 0.5R$ an all-triangles unstructured pattern is applied. This mesh arrangement in the pipe core is intended to avoid the wedge-shaped cells at the pipe axis which cause a significant unphysical time-step reduction. The total number of grid points of the LES mesh is 6×10^6 distributed as follows: in the outer region ($r \in [0.5R, 1.0R]$), $N_z = 256$, $N_\theta = 192$ and $N_r = 60$, being z the streamwise, θ the azimuthal and r the radial directions while in the inner region ($r \in [0, 0.5R]$), the unstructured mesh is also extruded in 256 planes. The grid spacings in wall units are $\Delta z^+ \approx 15$, $\Delta r\theta^+ \approx 16.5$ at $r = R$ and $\Delta r^+ \approx 1.2$ at the wall, being $\Delta y_1^+ \approx 0.6$. Concerning the WM setup, the WM/LES interface is placed at $y^+ \approx 150$, matching the top boundary nodes with their LES counterparts to avoid interpolation inaccuracies. The WM mesh is extruded in 20 layers and refined towards the wall, being the first off-wall node well into the viscous sublayer at a distance of $y_1^+ = 0.54$ and making a total amount of 9.8×10^5 inner nodes. Respecting the subgrid strategy for the LES domain, the dynamic Smagorinsky model has been used. Periodic boundary conditions are prescribed in the streamwise direction while no-slip and Neumann conditions are applied to the wall for velocity and pressure, respectively. The flow is enforced by keeping a constant mass flow consistent with the Reynolds number of $Re = 2R\overline{U}/\nu$ which is based on the bulk velocity $\overline{U}$. In this case $Re = 1.7 \times 10^4$ which corresponds to a $Re_\tau \approx 500$ according to the Blasius correlation.

To gain insight on the flow structures present in the WM/LES interface and their characteristic time-scales, the power spectrum of the streamwise

velocity component is computed in the WM/LES linking region (see Figure 3). This will provide valuable data about the temporal behavior of the resolved Reynolds stresses that are being introduced into the wall layer.

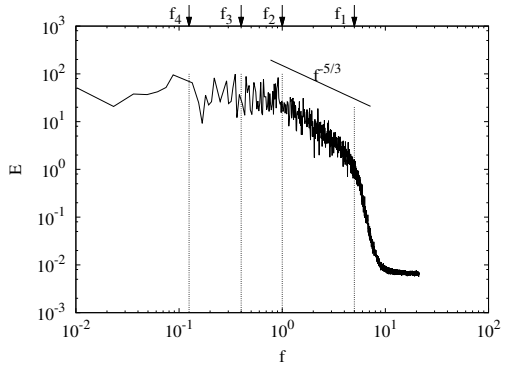

Figure 3: Power spectra of the streamwise velocity component at $y^+ \approx 150$ of a Pipe flow at $Re_\tau \approx 500$.

The characteristic flow frequencies revealed by the power spectrum will be used to determine the TAF filter lengths to be tested. Four frequencies have been selected in the plot. Firstly, two in the energy-containing range in which the largest flow structures are located, $f_1 = 0.125$ and $f_2 = 0.4$. The first one corresponds to the lowest frequency that can be captured by the present domain length. Then, other characteristic frequencies are considered by choosing the limit between the energy-containing and the inertial subrange, $f_3 = 1.0$, and the limit between the latter and the dissipation range, $f_4 = 5.0$. Therefore, the first test will be performed without filtering the LES input data. Then, successive filter lengths of $T_1 = 0.2$, $T_2 = 1.0$, $T_3 = 2.5$ and $T_4 = 8.0$, corresponding to the frequencies commented above ($T_n = 1/f_n$), will be applied in the WM/LES interface. Both, the averaging periods and

the frequencies are defined in terms of the non-dimensional time units (TU) and its inverse, respectively. In Table 1, the different filter configurations are summarized.

Table 1: Summary of the different filter configurations used for the TAF performance test. The tested filter lengths and their position in the energy spectrum are shown.

TAF Config.(n)	Filter length T_n	$f_n = 1/T_n$	Energy spectrum range
0	no filter	no filter	N/A
1	0.2	5.0	inertial/dissipation range limit
2	1.0	1.0	inertial/energy-containing range limit
3	2.5	0.4	within the energy-containing range
4	8.0	0.125	flow-through period, largest flow scales

Regarding the temporal integration and statistics averaging periods, the WRLES computation has been advanced during 100 flow-through cycles until reaching the statistically stationary regime. Once the steady state has been achieved, the WM has been coupled to the LES solution, and an additional transient period of $100\,TU$ has been run. Finally, the wall layer averaged variables have been collected along $100\,TU$ which is more than 10 times the largest flow structure appearing in the velocity spectrum.

3.2. Time-averaging filter performance test results

In Table 2, results concerning the Re_τ computed by the WM are given for each TAF configuration in Table 1. Each case is identified with a symbol to easily locate the test results in Figures 4 and 5.

Table 2: TAF performance test results performed with a channel flow at $Re_\tau \approx 500$. The WM computed Re_τ and its relative error with respect to the target value ($Re_\tau \approx 500$) is shown. Symbols are to identify the numerical results in Figures 4 and 5.

Test (n)	Symbol	Filter length T_n	Computed Re_τ	rel. err. [%]
0	○	no filter	528.70	5.74
1	△	0.2	515.66	3.13
2	▽	1.0	506.81	1.36
3	□	2.5	502.06	0.41
4	◇	8.0	502.18	0.43

On the other hand, in Figure 4, the mean velocity profiles for all TAF configurations are shown and compared with the DNS data of Chin *et al.*[41].

The tests confirm the findings of Cabot and Moin [13] about the incoming RRS. The excess of diffusivity due to the combination of a RANS model with the turbulent resolved inflow causes an overprediction of the wall shear stress, as the computed Re_τ value indicates in case 0 in which no measure was taken to avoid that. As the filter length is increased, the shear stress converges progressively to the reference Re_τ value. According to the values displayed in Table 2, satisfactory results are obtained when the cut-off filter length is set approximately at frequencies lower than inertial subrange ones. For higher frequencies (at the beginning of the dissipation range) the averaging period is not enough to sufficiently block the RRS inflow, although a significant improvement is observed compared to the non-filtered solution. Similar conclusions can be reached by inspecting the wall layer mean velocity profiles in Figure 4. Good convergence with the DNS solution is obtained when frequencies from the beginning of the inertial subrange upwards are

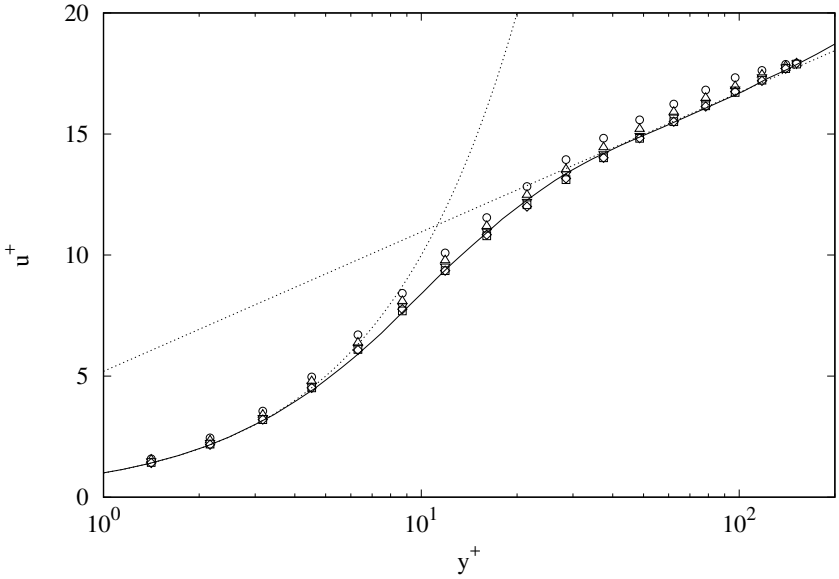

Figure 4: Mean streamwise velocity profiles of the wall layer region of a pipe flow at $Re_\tau \approx 500$. Comparison between DNS data (————) and the WM mean velocity field for five different TAF configurations (dots). ○ no TAF, △ $T_1 = 0.2\,TU$, ▽ $T_2 = 1.0\,TU$, □ $T_3 = 2.5\,TU$ and ◇ $T_4 = 8.0\,TU$. (See Table 2). The law of the wall (·····).

suppressed.

To analyze in deeper detail the effects of RRS inflow on the wall layer physics prediction, the ν_{Pa}/ν quantity is displayed in Figure 5 (left). The application of the TAF significantly reduces the apparent diffusive effects of the RRS in the wall domain, even with the smallest filter length. This is consistent with the fact that the smallest filtering period, $T_1 = 0.2$, suppresses the LES dissipation range frequencies. Nonetheless, for the smallest filter cut-off length, the total diffusivity levels are still too high. This unphysical extra diffusivity is indirectly caused by the remaining RRS through the WM

RANS model. This can be observed in Figure 5 on the right, in which the non-dimensional turbulent viscosity, ν_{Twm}/ν, is shown. According to the mixing-length-based RANS model (see Equation 13), the excessive levels of ν_{Twm} are due to an overpredicted value of the rate-of-strain tensor magnitude, $|S|$. This is a consequence of the incoming time-resolved velocity field of the inertial subrange, given that the RANS model expects only mean-flow-based quantities. On the other hand, the Van Driest wall-damping function could not cause the unphysical ν_{Twm} values, since erroneous values of y^+ derived from a wall shear stress overprediction, would shrink the function damping region towards the wall.

In summary, the highest frequencies are the main responsible for the apparent dissipative effects of the RRS. However, in the RANS context, filtering the smallest flow-scales and their dissipative component is not enough. The inertial subrange motions have an unphysical contribution to the rate-of-strain magnitude which leads to an incorrect evaluation of ν_T. For a RANS model, $|S|$ should be exclusively derived from the mean velocity field, or from very-large-scale unsteady motions at most[42]. Regarding the latter, according to the results, the lowest frequencies of the energy-containing range do not significantly affect the RANS model. For the largest filter lengths, $T_3 = 2.5$ and $T_4 = 8.0$, the results remain unchanged. As a conclusion, the minimum filter cut-off length has to be set at the energy-containing/inertial range limit.

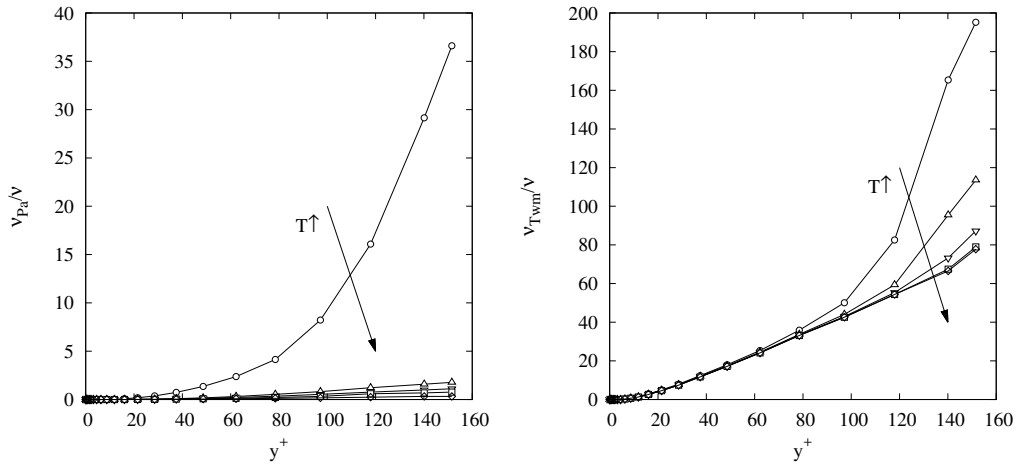

Figure 5: Left: Normalized viscosity obtained with the Park and Moin methodology as a measure of the the RRS levels ($\nu_{Pa}/\nu = -(R(\mathbf{U})S(\mathbf{U})/2\nu S(\mathbf{U})S(\mathbf{U})$ Right: Normalized turbulent viscosity (ν_{Twm}/ν). Both magnitudes are plotted vs. the wall distance in wall units and within the wall layer. See Table 2 for symbols definition.

4. Model validation

In this section, the proposed methodology is validated with two different cases, an equilibrium turbulent Pipe Flow at $Re_\tau \approx 3000$, and a non-equilibrium flow around a DU 91-W2-250 airfoil, at high Reynolds number and stall condition. Specifically, the flow conditions for the airfoil are, $Re = u_\infty c/\nu = 3 \times 10^6$, based on the airfoil chord (c) and the free stream velocity (u_∞), and an angle of attack (AoA) of 15.2°. The effects of the time averaging period on the numerical results will be analyzed by testing different T values, following the same methodology used in the previous section. The consequences of the filter length on unsteady flow conditions will be also studied through the analysis of boundary layer detachment/reattachment

frequencies in the stalled airfoil test.

The WMLES results will be compared with DNS data from Ahn *et al.*[43] for the Pipe Flow test, while experimental data from Timmer and van Rooij[44] will be used in the airfoil test for validation.

4.1. Pipe flow at $Re_\tau \approx 3000$

4.1.1. Test description

The DNS data of Ahn *et al.*[43] used for reference, corresponds to a Pipe Flow test at $Re_\tau = 3008$, and was obtained in a computational domain of length $30R$ with periodic conditions in the streamwise direction.

In our LES and WMLES computations, a 10R-long pipe has been used due to the large number of WM configurations to be tested. Despite that this domain length is insufficient to capture the very large structures that are engendered in Pipe and Channel flows at high Reynolds numbers[43], Lozano-Durán and Jiménez[45] showed that one-point statistics, which are the results analyzed below, remain unaffected with reasonably small domains. The authors[45] performed tests with a Channel flow at $Re_\tau = u_\tau \delta/\nu = 4200$ and a domain size of $L_x \times L_y \times L_z = 2\pi\delta \times 2\delta \times \pi\delta$, being x the streamwise, y the wall-normal, and z the spanwise directions, while δ is the channel half height. The channel length was about one third shorter than the present pipe flow simulation. Moreover, according to Ahn *et al.*[43], the effects of very large scales are more severe in Channel than in Pipe flows. This allows us to conclude that the length of $10R$ is large enough to evaluate the mean velocity profiles and the velocity fluctuations accurately.

The same procedure as in Section 3 has been followed to generate the computational grid. The total number of points of the LES mesh is 8.9×10^5

distributed as follows: a structured pattern for $r \in [0.5R, 1.0R]$ with $N_z = 128$, $N_\theta = 96$ and $N_r = 25$, while an all-triangle unstructured mesh is used in the pipe core. The grid spacings in wall units are $\Delta z^+ \approx 236$, $\Delta r\theta^+ \approx 198$ at $r = R$ and $\Delta r^+ \approx 60$, being the first off-wall LES nodes placed at $\Delta y_1^+ \approx 30$, at the beginning of the logarithmic region.

The tested TAF configurations are summarized in Table 3. The filter lengths, T, have been chosen through the energy spectrum of the streamwise velocity component obtained at the WM/LES interface ($y^+ \approx 210$), according to the methodology proposed in Section 3.

Table 3: Summary of the different TAF configurations tested with the $Re_\tau \approx 3000$ Pipe Flow.

TAF Config.(n)	Filter length T_n	$f_n = 1/T_n$	Energy spectrum range
0	no filter	no filter	N/A
1	0.125	8.0	dissipation range
2	0.55	1.8	inertial/dissipation range limit
3	2.0	0.5	inertial/energy-containing range limit
4	4.0	0.25	within the energy-containing range
5	10.0	0.1	flow-through period, largest flow scales

This numerical experiment, aside from evaluating the effects of the filter length T on the overall LES results, it is also intended to assess the ability of the TAF methodology in dealing with the LLM and the RRS inflow problems separately. To do so, the technique proposed by Kawai and Larsson [23] of extending the WM mesh to suppress the LLM will be used to uncouple the effects of the TAF on each specific problem. Therefore, the TAF configu-

rations detailed in Table 3, will be applied at two different WM extrusion heights, specifically, at $h_{wm}^{+} \approx 30$ and at $h_{wm}^{+} \approx 210$, which corresponds to the first and fourth off-wall node rows, respectively.

Thus, the WM grid resolution in the wall-normal direction is 10 layers when using an extrusion height of $h_{wm}^{+} \approx 30$, and 20 in case of $h_{wm}^{+} \approx 210$. The nodes are conveniently concentrated towards the wall according to a hyperbolic tangent law, being the position of the first off-wall nodes $y^{+} \approx 0.1$ in both cases, i.e., well into the viscous sublayer. The wall model cell count is 1.2×10^5 and 2.4×10^5, respectively.

The boundary conditions and the flow enforcement methodology are the same as in Section 3. In this case, the Reynolds number based on the bulk velocity is $Re = 1.33 \times 10^5$, which corresponds to $Re_\tau \approx 3026$ according to the Blasius correlation. Finally, a period of 100 flow-through cycles is computed to allow the flow to reach a statistically steady turbulent state, while the averaged variables are collected over 150 additional flow-through loops.

4.1.2. Test results

For convenience, from here onwards in this section, the notation followed by Ahn *et al.*[43] regarding the coordinate axis and velocity components will be used. The cylindrical coordinates are converted to Cartesian ones, being the new streamwise component $x = z$, the wall-normal direction $y = 1-r$ and the spanwise direction $z = r\theta$. Regarding the velocity components, $u = u_z$, $v = -u_r$ and $w = u_\theta$.

In Table 4, the computed Re_τ is shown for the six different TAF configurations specified in Table 3 at the two different extrusion heights. On the

other hand, in order to assess the overall improvement caused by the WM in the LES solution, a LES-only computation, which uses the same LES mesh as the WMLES but without WM, is also displayed. In brackets, the relative error of the computed Reynolds number with respect to the reference value of $Re_\tau \approx 3026$ is given.

Table 4: Computed Re_τ values of the pipe flow at $Re = 1.33 \times 10^5$ which corresponds to $Re_\tau \approx 3026$. The values are obtained for six different TAF filter lengths summarized in Table 3. Each TAF configuration is tested with a WM/LES interface height of $h^+_{wm} \approx 30$ and $h^+_{wm} \approx 210$. The LES-only solution is also displayed. The relative error in % with respect the reference value, $Re_\tau \approx 3026$, is in brackets.

TAF Config.(n)	Filter length T_n	No WM	WM $h^+_{wm} \approx 30$	WM $h^+_{wm} \approx 210$
0	No Filter	1923.6(36.4)	3409.2 (12.66)	3316.1 (9.58)
1	0.125	N/A	3305.6 (9.23)	3256.9 (7.63)
2	0.55	N/A	3201.1 (5.78)	3161.9 (4.49)
3	2.0	N/A	3141.3 (3.81)	3116.7 (3.0)
4	4.0	N/A	3138.0 (3.70)	3105.5 (2.62)
5	10.0	N/A	3135.6 (3.62)	3100.4 (2.45)

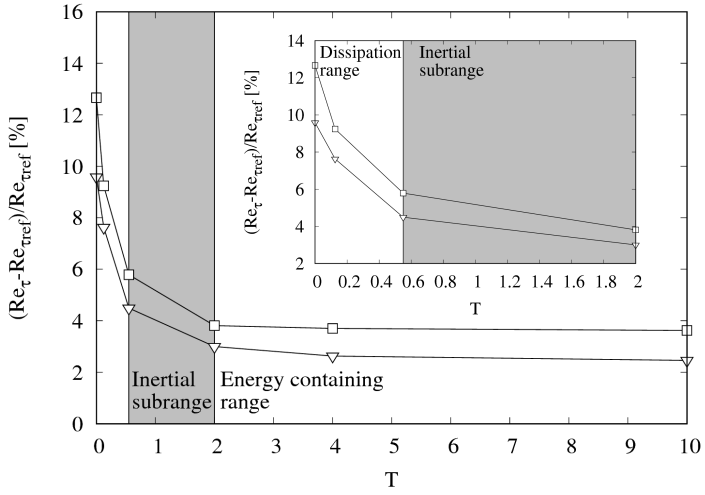

Figure 6: Relative error of the computed Re_τ in % with respect the reference value of $Re_\tau \approx 3026$ vs. the time-averaging period T. The values are obtained for the WM configurations in Table 4. $h_{wm}^+ \approx 30$ (□) and $h_{wm}^+ \approx 210$ (▽). On the top-right corner, the dissipation and the inertial subrange regions are zoomed.

In the same way as in the TAF performance test, the error in the wall shear stress prediction is minimized when frequencies in the inertial subrange or higher are filtered. For larger filtering lengths, the error keeps almost independent of T. On the other hand, the effects of the TAF on the LLM can be indirectly evaluated by analyzing the results obtained at the two different extrusion heights. When no TAF is applied, in the $h_{wm}^+ \approx 210$ test, the RRS inflow problem is isolated since the LLM error is avoided according to Kawai and Larsson's methodology [23]. By contrast, in the $h_{wm}^+ \approx 30$ test, both problems coexist. In the latter case, the error in the wall shear stress evaluation is approximately 3% higher than for the larger extrusion height. When applying the TAF, a significant drop of the Re_τ error is observed for

both tests. Nonetheless, the error difference narrows to only 1% for larger filter lengths, suggesting that in the $h_{wm}^{+} \approx 30$ case, the TAF is not only acting on the RRS inflow, but also on the LLM problem. It is worth to notice that the Kawai and Larsson's technique is slightly more efficient in tackling the LLM problem than Yang's one. However, the error difference is around only 1%, which according to our opinion, it does not justify the huge computational costs and geometrical difficulties associated to the use of Kawai and Larsson's approach.

In Figures 7, 8 and 9, plots of the mean streamwise velocity profile of the LES domain are displayed in wall units and logarithmic scale. The information is distributed as follows: in Figure 7, the gains of using an extended WM mesh are assessed by plotting WMLES results obtained for both extrusion heights, $h_{wm}^{+} \approx 30$ and $h_{wm}^{+} \approx 210$. To isolate the effects of the WM mesh height, the value of T has been set at $T_3 = 2.0$, in the inertial/energy-containing range limit, at which the effects of the RRS inflow are sufficiently minimized. Additionally, LES-only data is also displayed to evaluate the overall improvement obtained by using the WM in the optimal configuration.

On the other hand, Figures 8 and 9 are intended to analyze the influence of T on the mean velocity profile. The analysis is carried out separately for each extrusion heights, $h_{wm}^{+} \approx 30$ in Figure 8, and $h_{wm}^{+} \approx 210$ in Figure 9. The selected filter lengths correspond to the TAF configurations shown in Table 3 (from 0 to 3). For the sake of clarity, the largest averaging periods (configurations 4 and 5) are not displayed since they present minor differences with respect to configuration 3. In all plots, the DNS solution of Ahn *et al.*[43]

is displayed for comparison.

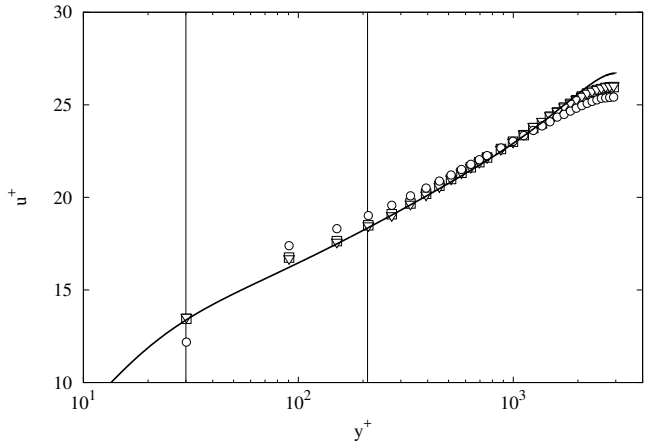

Figure 7: Mean streamwise velocity profiles in wall units . The wall distance is in logarithmic scale. The results have been obtained with the following configurations: LES-only ($\circ$), WMLES at $h_{wm}^+ \approx 30$ ($\square$) and WMLES at $h_{wm}^+ \approx 210$ ($\triangledown$). Both WMLES solutions are obtained with $T_3 = 2.0$. The vertical lines represent the two LES/WM interface heights. DNS Ahn *et al.*[43] (———).

According to data in Figure 7, with frequencies in the dissipation and inertial range suppressed, the WM is able to reproduce the characteristic logarithmic region for both extrusion heights. Although the higher extrusion height of $h_{wm}^+ \approx 210$ seems to perform slightly better than the lower configuration at $h_{wm}^+ \approx 30$, only minor differences are observed. On the other hand, in Figures 8 and 9, progressive improvements are obtained with rising values of T for both extrusion heights. Nonetheless, the gains are more significant in the $h_{wm}^+ \approx 30$ configuration. In this particular case, the non-filtered solution is simultaneously affected by the LLM and the RRS inflow problems, increasing the overall prediction error which is globally mitigated by the TAF. By

contrast, the velocity profile obtained with $h_{wm}^{+} \approx 210$, is only affected by the RRS inflow. In fact, the non-filtered solution obtained with Kawai and Larsson's method is reasonably good except for the first off-wall node, so that the impact of the TAF on the LES results was more limited than in the $h_{wm}^{+} \approx 30$ configuration.

As previously commented, the mean flow profile as well as the wall shear stress, remain constant for values of T larger than 2.0. This suggests that having a correct mean momentum balance is the primary requirement to obtain correct first-order statistics while having a realistic time-resolved wall shear stress is of relative importance. These results are in line with those obtained by Yang *et al.* [24], and they are consistent with the findings of Piomelli and Balaras [21], who showed that for poorly resolved wall regions, only the average effects of the near-wall structures must be represented by the wall layer model.

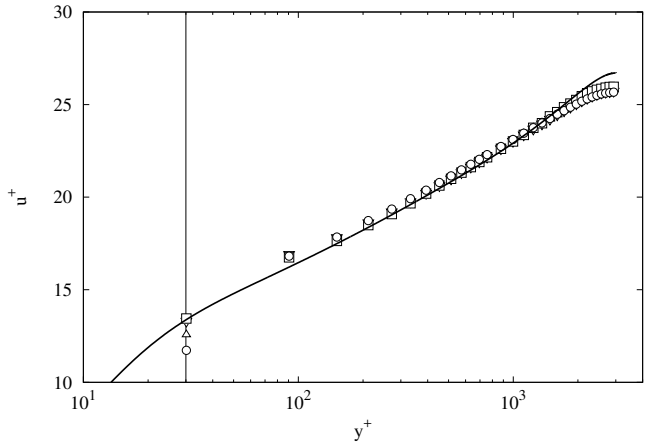

Figure 8: Mean streamwise velocity profiles in wall units. The wall distance is in logarithmic scale. The results have been obtained in the following conditions: WMLES at $h_{wm}^+ \approx 30$ without TAF (○) and with TAF with filtering periods of $T_1 = 0.125$ (△), $T_2 = 0.55$ (▽) and $T_3 = 2.0$ (□). See Table 3 for details. The vertical line represents the LES/WM interface position. DNS Ahn *et al.*[43] (———).

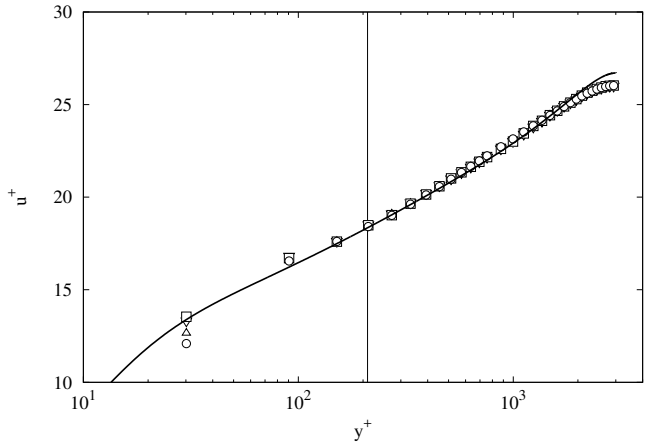

Figure 9: Mean streamwise velocity profiles in wall units. The wall distance is in logarithmic scale. The results have been obtained in the following conditions: WMLES at $h_{wm}^+ \approx 210$ without TAF (○) and with TAF with filtering periods of $T_1 = 0.125$ (△), $T_2 = 0.55$ (▽) and $T_3 = 2.0$ (□). See Table 3 for details. The vertical line represents the LES/WM interface position. DNS Ahn *et al.*[43] (———).

Finally, in Figure 10, the root-mean-square of the velocity fluctuations (u'_{rms}, v'_{rms} and w'_{rms}) as well as the Reynolds shear stress, $\langle u'v' \rangle$, is shown for the two extrusion heights, $h_{wm}^+ \approx 30$ (left) and $h_{wm}^+ \approx 210$ (right), with the same increasing values of T used for the mean streamwise velocity. Again, for a sufficiently large averaging period ($T \gtrsim 2.0$), the WMLES results converge to a very similar solution regardless of the WM height. The converged solutions are in fair agreement with the DNS reference except in the near-wall region, especially for the streamwise and the spanwise velocity fluctuations. This is due to the necessity of having a minimum amount of resolved scales to capture second-order statistics properly. Since the size of the eddies in the near-wall region is proportional to the wall distance and, therefore, very

small compared with those in the pipe center, the mesh is unable to capture a minimum amount of near-wall structures when using coarse meshes with a constant grid spacing. According to the results, it appears that the WM is not able to correct this. On the other hand, the velocity fluctuation results obtained with time averaging periods of 4.0 and 10.0 were very similar to those computed with $T_3 = 2.0$. This suggests that the fluctuation levels are more related to a well-predicted mean flow and a sufficiently fine mesh than having an accurate temporal resolution of the wall shear stress.

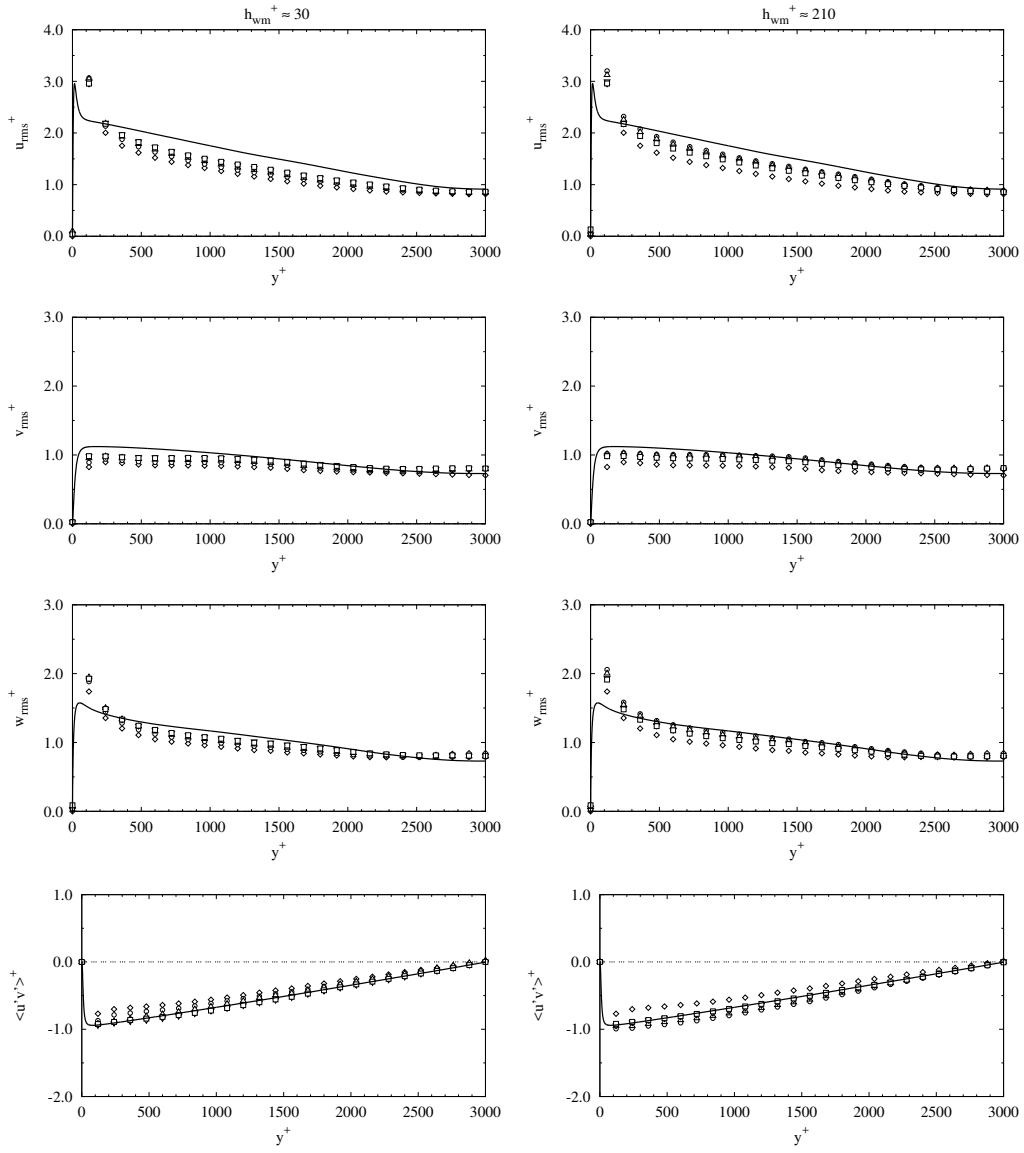

Figure 10: rms of the streamwise (u'^+_{rms}), wall-normal (v'^+_{rms}) and azimuthal (w'^+_{rms}) velocity fluctuations as well as the Reynolds shear stress ($\langle u'v' \rangle^+$) in wall units. The results have been obtained in the following conditions: LES-only ($\diamond$) and WMLES at $h^+_{wm} \approx 30$ (left) and $h^+_{wm} \approx 210$ (right). In case of WMLES, the wall model configurations are: no TAF ($\circ$), and TAF with filtering periods of $T_1 = 0.125$ ($\triangle$), $T_2 = 0.55$ ($\triangledown$) and $T_3 = 2.0$ ($\square$). See Table 3 for details. DNS Ahn *et al.*[43] (———).

4.2. Flow around a DU 91-W2-250 airfoil at Reynolds number $Re = 3 \times 10^6$ and $AoA = 15.2°$

4.2.1. Test description

The flow around a DU 91-W2-250 airfoil at high Reynolds number ($Re = 3 \times 10^6$) and in full stall ($AoA = 15.2°$), is studied to evaluate the WM performance in non-equilibrium conditions as well as to analyze the effects of the TAF averaging period on unsteady phenomena. In this particular case, the effects of T on the boundary layer detachment/reattachment frequency will be analyzed.

The DU 91-W2-250 profile is a wind turbine dedicated airfoil which is designed to have a premature laminar to turbulent transition to avoid performance degradation caused by dirtiness accumulation. It has been reported [26] that in the laminar portion of the boundary layer, the WM turbulence model must be switched off to obtain laminar profiles and, therefore, a more appropriate wall shear stress. However, a methodology to detect the laminar region has to be implemented, and this is out of the scope of the present work. For that reason, a profile with almost no laminar boundary layer section has been selected. On the other hand, wind tunnel data from Timmer and van Rooj[44] is available for comparison. It includes the integral lift and drag coefficients as well as the pressure coefficient distribution.

The computational domain of the simulation is a square region of $40c \times 40c \times 0.3c$, where x, y and z axis are the chord-wise, chord-normal and span-wise directions, respectively (see Figure 11). The leading edge of the airfoil is placed at the square center.

The airfoil simulation methodology has been taken from previous experi-

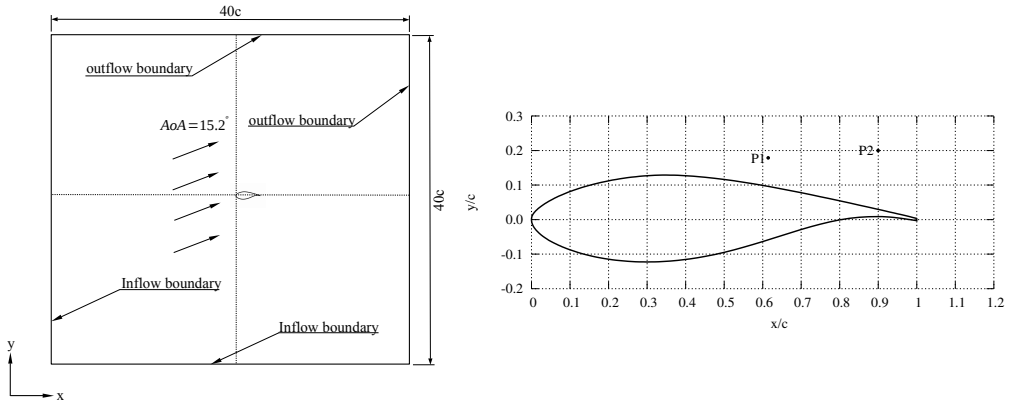

Figure 11: Left: Computational domain of the DU 91-W2-250 simulation at $Re = 3 \times 10^6$ and $AoA = 15.2°$. Right: DU 91-W2-250 geometry and position of probes P1 and P2.

ences in which numerical results and experimental data were compared obtaining good agreement between them [46]. To set an appropriate spanwise distance, L_z, the conclusions of the LESFOIL project [47] have been followed. In that project, LES simulations of an Aerospatiale A-airfoil at similar flow conditions (i.e., $AoA = 13.3°$ with flow separation and $Re = 2.1 \times 10^6$) were carried out. The authors concluded that a spanwise distance of approximately 1.5 times the flow separation distance in the wall-normal direction at the trailing-edge, was acceptable. According to preliminary computations which were subsequently confirmed, in the present case, the separation distance is approximately $0.2c$. Thus, a L_z of $0.3c$ has been set and further validated through two-point correlation in the spanwise direction. To do so, two numerical probes have been placed at maximum turbulent kinetic energy positions on the airfoil surface [48] and within the recirculation region, specifically at P1 $(0.61, 0.17)$ and P2 $(0.89, 0.20)$ (see Figure 11 right). The

two-point correlations have been computed according to Equation 16 for the fluctuations of the three velocity components and pressure:

$$\Re_{\phi\phi}(\mathbf{x}, \delta z) = \frac{\langle \phi'(\mathbf{x}, t)\phi'(\mathbf{x} + \delta z, t)\rangle}{\langle \phi'(\mathbf{x}, t)^2\rangle}, \tag{16}$$

where ϕ' is the fluctuation of any of the primitive variables, $\mathbf{x} = (x, y, z)$, and $\langle\cdot\rangle$ denotes averaging in time. In Figure 12, the $\Re_{\phi\phi}$ results are displayed for P1 and P2.

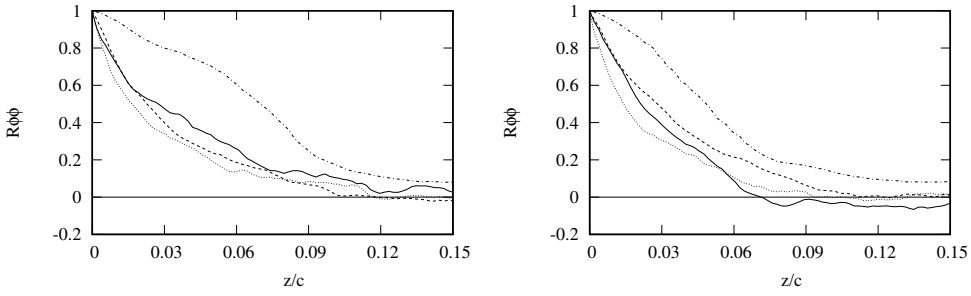

Figure 12: Two-point correlation of the three velocity components and pressure fluctuations along the spanwise direction. P1 left, and P2 right (see Figure 11 for probe positions). $\Re_{uu}$ (·····), $\Re_{vv}$ (———), $\Re_{ww}$ (- - - - -) and $\Re_{pp}$ (-·-·-·

control the first off-wall node distances properly. The 2D mesh has a resolution of 1.2×10^5 grid points; thus, the 3D mesh size is around 19.2×10^6 CVs. Since no experimental or WRLES data on boundary layer thickness was available, a preliminary LES computation was performed to estimate δ, being the smallest value approximately $\delta_{min} \approx 0.01c$ located at the airfoil leading edge. The quick transition to turbulence of this airfoil makes the boundary layer to thicken rapidly, reaching relatively high values of δ very close to the leading edge. The first off-wall LES nodes were placed at a wall distance of $y_1 = 0.0025c$, which is well inside the boundary layer but trying not to harm excessively the time-step size, Δt. The LES grid resolution parameters used by Park and Moin to perform WMLES of a NACA4412 airfoil[26] with mild flow separation have been followed. In their computation, the authors used space-averaged grid spacings of $\overline{\Delta x}^+ \approx 160$ and $\overline{\Delta z}^+ \approx 62$. On the other hand, the WM mesh has been generated by extruding 30 layers from the solid surface up to the first off-wall nodes at $y_1 = 0.0025c$. The layers are conveniently concentrated towards the wall to get an appropriate first off-wall node distance (i.e., $\Delta y_1^+ < 1$).

In Figure13, the grid spacings in the wall-normal and the two wall-parallel directions are displayed for both, the WM and the LES mesh. It has to be taken into account that the wall-parallel grid spacings are common for both grids. The local shear stress provided by the WM has been used to normalize the grid distances as much accurately as possible. The LES mesh has a poor resolution since the minimum value of Δy_1^+ is approximately 18. This is far away from the viscous sublayer, being impossible to capture the real flow dynamics, especially in the leading edge region where Δy_1^+ reaches a value of

almost 120. On the other hand, the WM mesh has a good resolution, with a Δy_1^+ below 0.4 throughout the solid surface. Regarding the grid spacing in the other directions, the stream and the spanwise resolutions range between $40 \lesssim \Delta x^+ \lesssim 200$ and $15 \lesssim \Delta z^+ \lesssim 80$, which is below the limits used by Park and Moin [26].

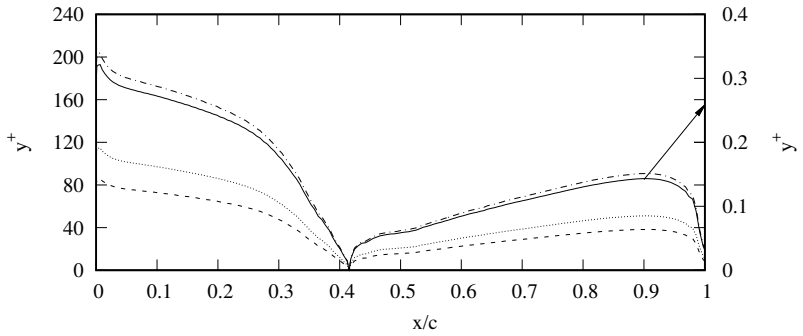

Figure 13: Left axis: Distributions of Δy_1^+ (·····), Δx^+ (-·-·-·) and Δz^+ (-----) of the LES mesh along the upper surface of a DU 91-W2-250 airfoil at $Re = 3 \times 10^6$ and $AoA = 15.2°$. Right axis: WM mesh Δy_1^+ (————).

Regarding the boundary conditions, a uniform velocity profile of magnitude u_∞ is set with the appropriate angle of attack at the inflow ($u = u_\infty cos(AoA)$, $v = u_\infty sin(AoA)$ and $w = 0.0$) while at the outflow boundary, a pressure-based condition is imposed. No-slip conditions on the airfoil surface are prescribed and finally, in the spanwise direction, periodic boundary conditions are used.

The same procedure as in previous sections has been followed to determine the temporal filtering periods to carry out the present study. The power spectrum of the streamwise velocity component has been obtained in the near-wall area within the boundary layer detached region. Its graph is

displayed in Figure 14 on the right, together with the selected TAF cut-off frequencies. In Table 5, the different TAF configurations are summarized. Time is measured in non-dimensional time units defined as $c/u_\infty = 1\,TU$. Unlike previous tests, the flow shows a significant large-scale unsteady behavior due to the boundary layer detachment/reattachment process, whose characteristic time-scale will be denoted as T_{dr}. Thus, the largest filtering period is selected to assess the effects of suppressing the contribution of the biggest flow motions to the wall shear stress in non-equilibrium unsteady conditions.

Table 5: Summary of the different TAF configurations tested with the flow around a DU 91-W2-250 airfoil at $Re = 3 \times 10^6$ and $AoA = 15.2°$.

Config.(n)	Filter length T_n	$f_n = 1/T_n$	Energy spectrum range
0	no filter	no filter	N/A
1	0.1	10.0	inertial/dissipation range limit
2	4.0	0.25	inertial/energy-containing range limit ($T_2 \approx 0.27T_{dr}$)
3	10.0	0.1	large fraction of the largest time-scale ($T_3 \approx 0.7T_{dr}$)

The time-averaged statistics have been collected along $80\,TU$ with a transient period of $30\,TU$. These intervals were obtained by analyzing the instantaneous lift coefficient shown in Figure 14 on the left, corresponding to the simulation performed with a filtering period of $T_2 = 4.0$. According to the $C_l(t)$ chart, the initial transient perturbations vanish at $t \approx 30\,TU$. On the other hand, since the instantaneous C_l is closely related to the detachment/reattachment process of the boundary layer, the power spectrum of its signal has been used to determine the characteristic time-scale of the

largest and most energetic motions, T_{dr}, whose value is $14.49\,TU$. Therefore, the total averaging period of $80\,TU$ represents approximately six detachment/reattachment cycles.

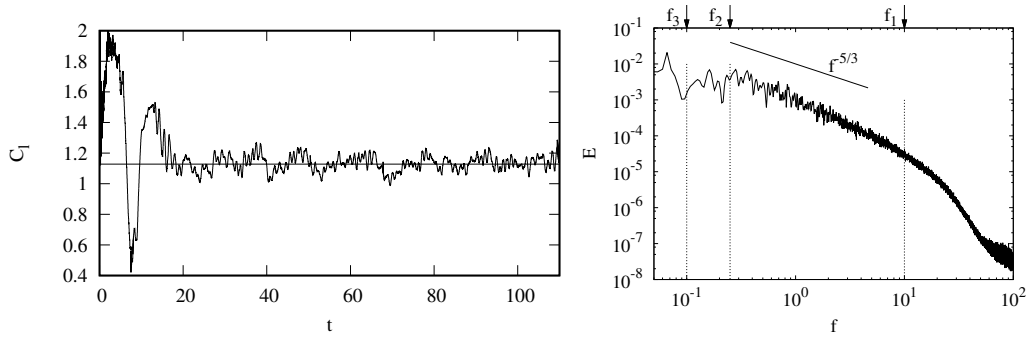

Figure 14: Left: Instantaneus lift vs. time in dimensionless TU. The horizontal continuous line represents the experimental average value[44] of $C_l = 1.128$. Right: Energy spectrum of the streamwise velocity component obtained at a near-wall position in the recirculation region.

Based on the preliminary LES computation used for the approximation of δ, an estimation of the grid resolution needed at the wall for a WRLES was done. This allowed making a projection of the diffusive CFL upper bound for the time-step as well as of the total number of grid points, N_{cv}, resulting in $dt \approx 4 \times 10^{-6}$ and $N_{cv} \approx 100$ million, respectively. This is one order of magnitude more regarding the grid size and two orders of magnitude for the time-step, compared to the WMLES. These values are in line with other studies [26].

4.2.2. Test results

In Figure 15, LES-only and WMLES results of the time-averaged pressure coefficient, $C_p = 2(p - p_\infty)/\rho u_\infty^2$, are shown together with experimental data of Timmer and van Rooij [44]. WMLES computations have been carried out according to the TAF configurations summarized in Table 5. For the sake of clarity, configuration 1 results are not shown since they are very similar to those of configuration 3.

On the other hand, in Figure 16, numerical results of skin friction distribution in the streamwise direction, $C_{fx} = 2\tau_{wx}/\rho u_\infty^2$, obtained in the same conditions as the C_p, are plotted for the upper surface.

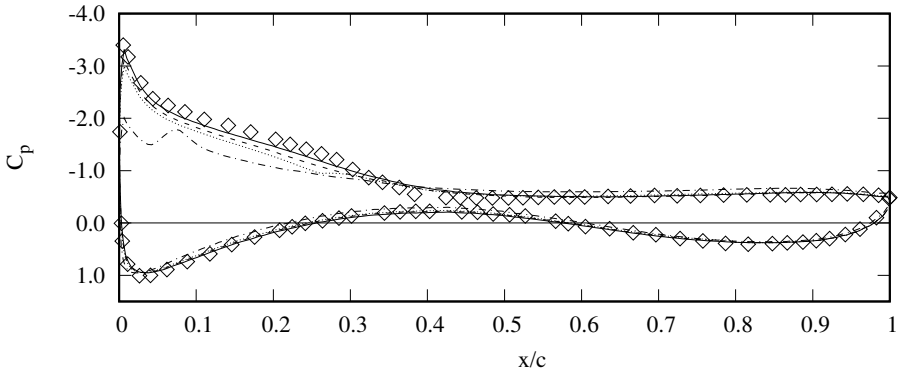

Figure 15: Pressure coefficient distribution along the upper and lower surface of a DU 91-W2-250 airfoil at $Re = 3 \times 10^6$ and at $AoA = 15.2°$. LES-only results (-·-·-·-·-), non-filtered WMLES (·····), WMLES with $T_2 = 4.0$ (————), and WMLES with $T_3 = 10.0$ (------). Experimental data [44] (◇).

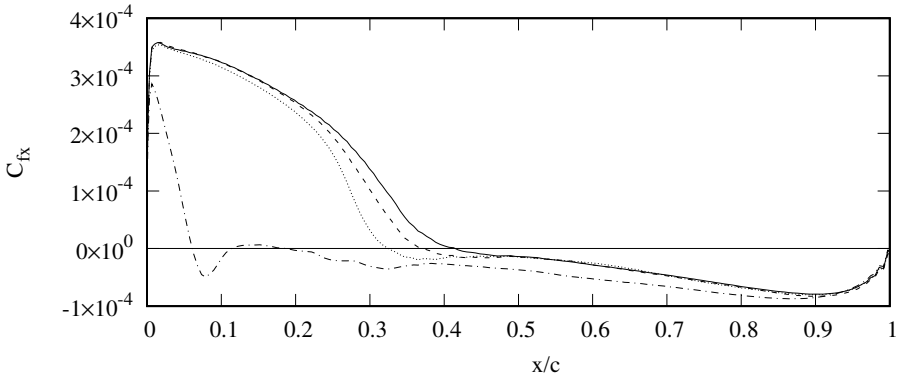

Figure 16: Skin friction coefficient distribution in the streamwise direction, C_{fx}, along the upper surface of a DU 91-W2-250 airfoil at $Re = 3 \times 10^6$ and at $AoA = 15.2°$. LES-only results (-·-·-·), non-filtered WMLES (·····), WMLES with $T_2 = 4.0$ (————), and WMLES with $T_3 = 10.0$ (------).

Good agreement between experimental and numerical results are obtained for the C_p when the WM filtering period is set at $T_2 = 4.0$. This filter length corresponds to the energy-containing/inertial range limit while representing a relatively small fraction of the largest flow time-scale, T_{dr}, specifically, $T_2 \approx 0.27 T_{dr}$. As in the Pipe Flow tests, poor results are obtained if higher frequencies are not filtered. However, unlike in equilibrium conditions, deficient predictions are also obtained when the lowest frequencies associated with the largest and most energetic flow scales are suppressed. Specifically, for $T_3 = 10.0$, which is approximately 0.7 times T_{dr}, the numerical C_p becomes underpredicted with respect to the experimental reference.

Regarding the skin friction coefficient, no experimental data is available for comparison. Nonetheless, the C_{fx} curve obtained with a filter length of $T_2 = 4.0$ shows a consistent behavior with respect to the experimental C_p.

In this case, the skin friction becomes negative at the same position where the experimental C_p curve shows the beginning of the pressure plateau (i.e., around $x/c \approx 0.43$). These two particularities in the C_{fx} and C_p curves are associated with the boundary layer detachment point, which suggests that the C_{fx} is well predicted at least from a qualitative point of view.

The consequences of using an inadequate filtering period seem to be concentrated in the flow detachment point region. Significant discrepancies in the C_{fx} predictions are observed in this region when different averaging periods are used, while almost identical results are obtained towards the airfoil edges. This is because the instantaneous position of the detachment point varies significantly in time due to the boundary layer detachment/reattachment process. This causes a strongly unsteady behavior of the instantaneous skin friction in that region, with a characteristic fluctuating period of T_{dr}. By contrast, at the airfoil ends, the skin friction seems to have a more constant value, at least in the leading edge area, making the results in these regions more insensitive to T. These observations suggest that the unsteady component of the skin friction derived from very-large-scale motions play an essential role on the flow global behavior. A sufficiently small averaging period allowing to capture these effects must be used.

On the other hand, in Table 6, the integral values of the drag and the lift coefficients ($C_d = 2D/\rho u_\infty A$, $C_l = 2L/\rho u_\infty A$, where D and L are the total aerodynamic forces in the stream-normal and the streamwise directions and A is the airfoil surface) are presented and compared with the experimental data. For the drag coefficient, the viscous and the pressure components are shown together with its total value. The numerical results are obtained in

the same conditions as the C_p and C_{fx} plots presented above. The conclusions derived from the pressure and skin friction coefficients are confirmed with the integral magnitudes. A slight discrepancy between the numerical C_d at $T_2 = 4.0$ and the experimental reference is observed. According to the two-point correlations in Figure 12, there is no need for a wider computational domain. Thus, the remaining discrepancy could be caused by the geometrical differences between the experimental and the numerical domains which feature completely different external boundaries.

Table 6: Lift and drag coefficient values of a DU 91-W2-250 airfoil at $Re = 3 \times 10^6$ and at $AoA = 15.2°$ obtained with and without WM together with experimental data [44]. The WMLES results have been obtained with the TAF configurations summarized in Table 5. The relative differences between the numerical and the experimental data are shown in %.

Model	Filter-length T	C_l	rel. diff. [%]	C_d (press.)	C_d (visc.)	C_d (total)	rel. diff. [%]
Experimental	N/A	1.128	–	–	–	0.1144	–
LES-only	N/A	0.932	17.37	0.2063	1.79×10^{-4}	0.2064	80.41
WMLES	No Filter	1.030	8.68	0.1503	2.30×10^{-4}	0.1505	31.55
WMLES	0.1	1.080	4.25	0.1353	2.46×10^{-4}	0.1355	18.44
WMLES	4.0	1.123	0.44	0.1298	2.52×10^{-4}	0.1300	13.63
WMLES	10.0	1.061	6.02	0.1408	2.44×10^{-4}	0.1410	23.25

Finally, in Table 7, the boundary layer detachment/reattachment characteristic periods, T_{dr}, are shown. The objective is to analyze the influence of the wall shear stress temporal resolution on the unsteady dynamics of large-scale motions. According to obtained results, the characteristic periods are affected by the filter length T. Nonetheless, it is unclear whether the dispersion of T_{dr} results is a consequence of a poorly resolved mean flow, or

the averaging period directly conditions its value. Although there is a correlation between T and T_{dr} (the larger the filter length, the larger the flow characteristic time-scale), by comparing LES-only and WMLES results, it can be concluded that having a well-predicted mean flow strongly influences the T_{dr} value.

Table 7: Detachment/reattachment characteristic time-scales (T_{dr}) of a flow around a DU 91-W2-250 airfoil at $Re = 3 \times 10^6$ and $AoA = 15.2°$. Results are obtained for LES-only and WMLES computations. In case of WMLES the TAF configurations in Table 5 have been used.

Model	Filter-length T	Char. time-scale T_{dr}
LES-only	N/A	8.33
WMLES	No Filter	12.25
WMLES	0.1	12.34
WMLES	4.0	14.49
WMLES	10.0	15.87

5. Conclusions

A general and efficient WM for incompressible LES and suitable for unstructured meshes is presented and validated through different tests including strongly unsteady non-equilibrium flows. The present methodology is included in the two-layer model family of wall shear stress models[10], and to the authors' best knowledge, it uses for the first time the full incompressible URANS equations as a mathematical and physical model. This mathematical approach has been selected given the importance of the non-equilibrium terms (i.e., advective and pressure gradient) when dealing with complex flow

phenomena such as boundary layer detachment, adverse pressure gradients or flow recirculations.

Wall shear stress models in general and RANS-based WMs in particular, are affected by the "log-layer mismatch" and the resolved Reynolds stresses inflow problems which undermine the quality of the WM numerical predictions.

In the present work, a time-averaging filter for the LES variables is applied in the WM/LES interface to tackle both issues at once with a single-step and low-computational-cost technique suitable for any geometry. While the TAF strategy has already been applied to address the LLM problem[24], it is used for the first time to block the RRS inflow in the TLM context. According to the obtained results, this approach is extremely efficient in avoiding the RRS inflow consequences, and combined with its effects on the LLM, it dramatically reduces the complexity of the WM formulation and implementation while strongly increasing its efficiency and geometrical range of applicability compared to existing TLM strategies[26].

The proposed methodology has been validated with two equilibrium Pipe Flow tests at $Re_\tau \approx 500$ and $Re_\tau \approx 3000$, and a non-equilibrium flow around a DU 91-W2-250 airfoil at $Re = 3 \times 10^6$ in full stall. As recurrently observed in all these tests, the signal of the LES variables must be filtered with a sufficiently large temporal filter length before being used as boundary condition for the WM RANS-based domain. Specifically, frequencies higher than the energy-containing/inertial range limit must be suppressed. While the apparent diffusive effects inherent to the resolved smallest scales are almost completely avoided with smaller filter lengths, it is found that the RANS

model provides excessive diffusivity when inertial subrange frequencies are introduced through the boundary. The URANS approach exclusively resolves the mean flow evolution or the very-large structure unsteady component at most. Thus, for any RANS formulation, the turbulent viscosity should be derived from the mean flow, which is supposedly the only available data. When time-resolved turbulent motions are introduced through the boundary, they cause the RANS model to work out of its range of applicability, causing a prediction failure.

On the other hand, unlike in equilibrium conditions, for non-equilibrium unsteady flows, it also exists an upper bound for the TAF filter length. It is found that the largest flow structures contribution to the instantaneous skin friction plays an important role in regions with a strong unsteady behavior. Therefore, a sufficiently small filter length allowing to capture large-scale temporal effects must be used. In the particular case of the flow around a DU 91-W2-250 airfoil, a TAF averaging period corresponding approximately to a quarter of the largest flow time-scale allowed to obtain accurate predictions.

Additionally, it is found that the filtering period affects the large-scale characteristic frequencies. However, it remains unclear whether the value of T directly influences the largest time-scales, or this is an indirect consequence of having a poorly resolved mean flow.

Finally, another important conclusion of the present work is that the increase of the time-step upper bound in explicit computations has a huge potential in cutting down the computational costs for high Reynolds number flows. Probably, even more than the reduction of LES near-wall spatial resolution requirements since it is very difficult to parallelize the advancement

in time. In order to support this idea, a new set of expressions for the total computational cost Reynolds number scaling which takes into account the time integration efforts is proposed. Further research on methodologies intended to mitigate the time-step effects are part of our research plans.

6. Acknowledgments

This work has been financially supported by the Ministerio de Economía y Competitividad, Spain (ENE2014-60577-R and ENE2017-88697-R), the Government of Catalonia, Agència de Gestió d'Ajuts Universitaris i de Recerca (2010-TEM-00098), a Ramón y Cajal postdoctoral contract (RYC-2012-11996) and the Barcelona Supercomputing Center by granting computational resources for the DU 91-W2-250 tests (FI-2017-1-0019). The authors thankfully acknowledge these institutions. Special thanks to Junsun Ahn and Hyung Jin Sung for providing results that allowed comparison in the pipe flow at $Re_\tau \approx 3000$ test.

[1] U. Piomelli, Wall-layer models for large-eddy simulations., Prog. Aerosp. Sci. 44 (2008) 437–446.

[2] D. R. Chapman, Computational aerodynamics, development and outlook, AIAA J. 17 (1979) 1293–1313.

[3] H. Choi, P. Moin, Grid-point requirements for large eddy simulation: Chapman's estimates revisited., Phys. Fluids 24 (2012) 011702.

[4] Q. Wang, S. Gomez, P. Bloniganc, A. Gregoryd, E. Qiane, Towards scalable parallel-in-time turbulent flow simulations., Phys. Fluids 25 (2013) 110818.

[5] R. Verstappen, A. Veldman, Direct numerical simulation of turbulence at lower costs., J. Eng. Math. 37 (1997) 143–159.

[6] J. W. Deardorff, A numerical study of three-dimensional turbulent channel flow at large Reynolds numbers., J. Fluid Mech. 41 (1970) 453–480.

[7] F. X. Trias, O. Lehmkuhl, A self-adaptive strategy for the time-integration of Navier-Stokes equations., Numer. Heat Tr. B-Fund. 60-2 (2011) 116–134.

[8] P. R. Spalart, Detached-eddy simulation., Annu. Rev. Fluid Mech. 41 (2009) 181–202.

[9] E. Balaras, C. Benocci, Subgrid-scale models in finite-difference simulations of complex wall bounded flows., in: AGARD CP 551, 1994, pp. 2.1–2.5.

[10] E. Balaras, C. Benocci, U. Piomelli, Two-layer approximate boundary conditions for large-eddy simulations., AIAA J. 34 (6) (1996) 1111–1119.

[11] H. Werner, H. Wengle, Large-eddy simulation of turbulent flow over and around a cube in a plate channel., in: Turbulent Shear Flows, Vol. 8, Springer-Verlag, 1993.

[12] W. Cabot, Near-wall models in large-eddy simulations of flow behind a backward-facing step., Annual Research Brief. Center for Turbulence Research, Stanford, CA (1996) 199–210.

[13] W. Cabot, P. Moin, Approximate wall boundary conditions in the large-

eddy simulation of high Reynolds number flow., Flow Turbul. Combust. 63 (1999) 269–291.

[14] S. B. Pope, Turbulent flows., Cambridge Univesity Press, 2000.

[15] M. Wang, P. Moin, Dynamic wall modelling for large-eddy simulation of complex turbulent flows., Phys. Fluids 14(7) (2002) 2043–2051.

[16] F. Tessicini, L. Temmerman, M. A. Leschziner, Approximate near-wall treatments based on zonal and hybrid RANS-LES methods for LES at high Reynolds numbers., Int. J. Heat Fluid Fl. 27(5) (2006) 789–799.

[17] F. Tessicini, N. Li, M. A. Leschziner, Large-eddy simulation of three-dimensional flow around a hill-shaped obstruction with a zonal near-wall approximation., Int. J. Heat Fluid Fl. 28 (2007) 894–908.

[18] S. Kawai, K. Asada, Wall-modeled large-eddy simulation of high Reynolds number flow around an airfoil near stall condition., Comput. Fluids 85 (2013) 105–113.

[19] V. G. Diurno, E. Balaras, U. Piomelli, Wall-layer models for LES of separated flows., Modern Simulation Strategies for Turbulent Flows, ed. B. Geurts. Philadelphia, PA: RT Edwards (2001) 207–222.

[20] P. R. Spalart, S. Allmaras, A one-equation turbulence model for aerodynamic flows., La Recherche Aerospatiale 1 (1994) 5–21.

[21] U. Piomelli, E. Balaras, Wall-layer models for large-eddy simulations., Annu. Rev. Fluid Mech. 34 (2002) 349–374.

[22] S. Kawai, J. Larsson, A dynamic wall model for large-eddy simulations of high Reynolds number compressible flows., Annual Research Brief. Center for Turbulence Research, Stanford, CA (2010) 25–37.

[23] S. Kawai, J. Larsson, Wall-modeling in large eddy simulation: Length scales, grid resolution, and accuracy., Phys. Fluids 24 (2012) 015105.

[24] X. I. A. Yang, G. I. Park, P. Moin, Log-layer mismatch and modeling of the fluctuating wall stress in wall-modeled large-eddy simulations., Phys. Rev. Fluids 2 (2017) 104601.

[25] S. Kawai, J. Larsson, Dynamic non-equilibrium wall-modeling for large eddy simulation at high Reynolds number., Phys. Fluids 25 (2013) 015105.

[26] G. I. Park, P. Moin, An improved dynamic non-equilibrium wall-model for large eddy simulation., Phys. Fluids 26 (2014) 015108.

[27] J. Larsson, S. Kawai, J. Bodart, I. Bermejo-Moreno, Large-eddy simulation with modeled wall-stress: recent progress and future directions., Mech. Engng. Rev. 3(1) (2016) 1–23.

[28] S. Patil, D. Tafti, Wall modeled large eddy simulations of complex high Reynolds number flows with synthetic inlet turbulence., Int. J. Heat Fluid Fl. 33 (2012) 9–21.

[29] J. Bodart, J. Larsson, Wall-modeled large-eddy simulation in complex geometries with application to high-lift devices., Annual Research Brief. Center for Turbulence Research, Stanford, CA (2011) 37–48.

[30] J. Bodart, J. Larsson, Sensor-based computation of transitional flows using wall-modeled large-eddy simulation., Annual Research Brief. Center for Turbulence Research, Stanford, CA (2012) 229–240.

[31] P. Moin, K. Squires, W. Cabot, S. Lee, A dynamic subgrid-scale model for compressible turbulence and scalar transport., Phys. Fluids 3 (1991) 2746.

[32] D. K. Lilly, A proposed modification of the Germano subgrid-scale closure method., Phys. Fluids 4 (1992) 633–635.

[33] L. Jofre, O. Lehmkuhl, J. Ventosa, F. X. Trias, A. Oliva, Conservation properties of unstructured finite-volume mesh schemes for the Navier-Stokes equations., Numer. Heat Tr. B-Fund. 65 (2014) 53–79.

[34] F. X. Trias, O. Lehmkuhl, A. Oliva, C. D. Pérez-Segarra, R. Verstappen, Symmetry-preserving discretization of Navier-Stokes equations on collocated unstructured grids., J. Comput. Phys. 258 (2014) 246–267.

[35] L. Paniagua, O. Lehmkuhl, C. Oliet, C. Pérez-Segarra, Large eddy simulations (LES) on the flow and heat transfer in a wall-bounded pin matrix., Numerical Heat Transfer, Part B: Fundamentals 65(2) (2014) 103–128.

[36] R. W. C. P. Verstappen, A. E. P. Veldman, Symmetry-preserving discretization of turbulent flow., J. Comput. Phys. 187 (2003) 343–368.

[37] X. I. A. Yang, J. Sadique, R. Mittal, C. Meneveau, Integral wall model for large eddy simulations of wall-bounded turbulent flows., Phys. Fluids 27 (2015) 025112.

[38] A. Carmona, O. Lehmkuhl, C. D. Pérez-Segarra, A. Oliva, Numerical analysis of the transpose diffusive term for viscoplastic-type non-newtonian fluid flows using a collocated variable arrangement., Numer. Heat Tr. B-Fund. 67 (2015) 410–436.

[39] G. I. Park, P. Moin, Numerical aspects and implementation of a two-layer zonal wall model for LES of compressible turbulent flows on unstructured meshes., J. Comput. Phys. 305 (2016) 589–603.

[40] Termo Fluids S.L., web page: http://www.termofluids.com.

[41] C. Chin, A. S. H. Ooi, I. Marusic, H. M. Blackburn, The influence of pipe length on turbulence statistics computed from direct numerical simulation data., Phys. Fluids 22 (2010) 115107.

[42] S. Lardeau, M. Leschziner, Unsteady Reynolds-Averaged Navier-Stokes computations of transitional wake/blade interaction., AIAA J. 42(8) (2004) 1559–1571.

[43] J. Ahn, J. H. Lee, J. Lee, J. H. Kang, H. J. Sung, Direct numerical simulation of a 30R long turbulent pipe flow at $\mathrm{Re}_\tau = 3008$., Phys. Fluids 27 (2015) 065110.

[44] W. A. Timmer, R. P. J. O. M. Van Rooij, Summary of the Delft university wind turbine dedicated airfoils., J. Sol. Energ. 125 (2004) 1–11.

[45] A. Lozano-Durán, J. Jiménez, Effect of the computational domain on direct simulations of turbulent channels up to $\mathrm{Re}_\tau = 4200$., Phys. Fluids 26 (2014) 011702–1.

[46] I. Rodríguez, O. Lehmkuhl, R. Borrell, A. Oliva, Direct numerical simulation of a NACA0012 in full stall., Int. J. Heat Fluid Flow 43 (2013) 194–203.

[47] C. P. Mellen, J. Fröhlich, W. Rodi, Lessons form LESFOIL project on large-eddy simulation of flow around an airfoil., AIAA J. 41-4 (2003) 573–581.

[48] K. Asada, S. Kawai, Large-eddy simulation of airfoil flow near stall condition at Reynolds number 2.1×10^6., Phys. Fluids 30 (2018) 085103.